Novel NASICON-typed porous $Ni_{1.5}V_2(PO_4)_3$/C and $Mn_{1.5}V_2(PO_4)_3$/C as anode materials for lithium-ion batteries: Crystal structure and electrochemical lithiation/delithiation reaction mechanism

Mohja Amou [a], Badre Larhrib [b], Noha Sabi [c], Mohammed Srout [a], Ayalew H. Assen [d], Mohammed Mansori [a], Oleksandr Dolotko [c,e], Nouredine Oueldna [f], Hervé Martinez [b], Ismael Saadoune [a,d,*]

[a] *Cadi Ayyad University (UCA), IMED-Lab, Av. A. El Khattabi, P.B. 549, Marrakesh, Morocco*
[b] *Université de Pau et des Pays de l'Adour, E2S UPPA, CNRS, IPREM, Pau, France*
[c] *Karlsruhe Institute of Technology (KIT), Institute for Applied Materials-Energy Storage Systems (IAM-ESS), Hermann-von-Helmholtz-Platz 1, D-76344 Eggenstein-Leopoldshafen, Karlsruhe, Germany*
[d] *Applied Chemistry and Engineering Research Centre of Excellence (ACER CoE), Mohammed VI Polytechnic University, Lot 660, Hay Moulay Rachid, Ben Guerir 43150, Morocco*
[e] *Helmholtz-Institute Ulm for Electrochemical Energy Storage (HIU), P.O. Box 3640, D-76021 Karlsruhe, Germany*
[f] *IM2NP, Aix-Marseille University, Faculté des Sciences de Saint-Jérôme case 142, 13397 Marseille, France*

Keywords:
NaSICon
XPS
Operando
Jahn-Teller distortion
Energy storage
Batteries

A B S T R A C T

Novel porous NaSICon-typed phosphate materials $Ni_{1.5}V_2(PO_4)_3$/C (NVP/C) and $Mn_{1.5}V_2(PO_4)_3$/C (MVP/C) are introduced as anode materials for Li-ion batteries. The materials were prepared via sol-gel method with annealing under argon flow. The structural, morphological, and electrochemical investigations of the materials as anodes for Li-ion batteries were conducted. The samples crystallized in a distorted triclinic system with a $P\bar{1}$ space group. The two synthesized anode materials exhibited a conversion mechanism, displaying reversible initial charge capacities of 495 mAh.g^{-1} and 550 mAh.g^{-1} at 0.2C rate for NVP/C and MVP/C, respectively. Both materials showed better cycling stability at high rates and good rate capability performances with high coulombic efficiencies. For long term cycling, the materials can maintain a good reversible capacity for 1000 cycles, although a continuous decrease was noticed during the first cycles. The structural changes and the SEI growth impacting the electrochemical performances of the materials were evidenced via *in* operando XRD and X-ray photoelectron spectroscopy, leading to the understanding of the lithiation/delithiation reaction mechanism involved in the studied phosphates.

1. Introduction

Over the last decades, Li-ion batteries (LIBs) have been considered as the principal, unrivaled, and most efficient energy storage systems. Despite the progress that this technology has known, the electrochemical performance of current commercialized LIBs is unable to meet the new requirements of the growing energy demands [1]. The development of high-performing electrode materials becomes a necessity. At this time, the vast majority of LIBs available in the market mainly rely on graphite as an anode material. However, graphite suffers from several issues, such as limited specific capacity (372 mAh.g ^{1}), poor rate capability, and safety concerns [2]. Consequently, safer, cost-effective, and environmentally benign anode materials with high energy density should be developed. To face these challenges, various materials were explored, including polyanionic NaSICon phosphate-based compounds. These materials are thermodynamically stable and the presence of the polyanion $(PO_4)^3$ strengthens the transition metal-oxygen bonds present in compounds avoiding any potential oxygen release from the electrode material. Additionally, $(PO_4)^3$ improves ionic conductivity through providing 3D channels for rapid diffusion of Li^+ [3,4].

$LiTi_2(PO_4)_3$ was the first NaSICon-structured material reported as an anode for LIBs by Delmas et al. [5]. The material crystallizes in the

* Corresponding author at: Cadi Ayyad University (UCA), IMED-Lab, Av. A. El Khattabi, P.B. 549, Marrakesh, Morocco.
E-mail address: i.saadoune@uca.ma (I. Saadoune).

rhombohedral system with $R\bar{3}c$ space group, and further investigation demonstrated that it exhibits a two-phase mechanism during the discharge-charge process. Following the same trend, numerous Ti-based NaSICon phosphates were investigated as potential negative electrodes [6,7]. However, titanium assures the transfer of only one electron through its redox couple Ti^{4+}/Ti^{3+} during discharge-charge process with a working voltage close to 1 V. Conversely, vanadium is known for its multiple valences, and the possibility of reducing V^{3+} to lower valences allows V-based materials to be applied as anodes. Therefore, the switch towards V-based NaSICon phosphates became a preference.

$Li_3V_2(PO_4)_3$ was demonstrated to operate as an anode material owing to the redox couple V^{3+}/V^{2+} whether in a rhombohedral form (r-LVP) [8,9] or monoclinic form (m-LVP) [10]. Nevertheless, there are several challenges surrounding this material. While the highest capacity reported for the m-LVP as an anode material was 162 mAh.g ^{1}, in a potential range of 1.0–3.0 V [11], the r-LVP could only be synthesized via ion exchange reaction on sodium counterpart $Na_3V_2(PO_4)_3$ (NVP), which is more thermodynamically stable [9].

In a previous work, the investigation of $Fe_{1.5}V_2(PO_4)_3$/C as an anode revealed that this material, crystallizing in $P\bar{1}$ space group, exhibits a conversion mechanism. It displays an exceptional cycling behavior with high reversible specific capacity, starting from the second cycle, reaching 600 mAh.g ^{1} and high stability at long term cycling in a large potential range of 0.01–3.0 V [12]. To the best of our knowledge, there are no electrochemical studies reporting V-based NaSICon phosphates with transition metals Mn, Fe, and Ni as anode materials for LIBs. In other research works, it was demonstrated that the involvement of nickel in anode materials contributes to the charge transfer of Li^+ ions and the reduction of polarization [13]. Thus, the reversibility of the specific capacity and discharge rate were improved. Moreover, manganese's ability of self-polarization, and capability of enhancing ionic conductivity and electrochemical reaction kinetics [14], make this transition metal a worthy choice for perspective anode materials.

Herein, two novel NaSICon-typed materials $Ni_{1.5}V_2(PO_4)_3$/C and $Mn_{1.5}V_2(PO_4)_3$/C are explored. The synthesis conditions, structural and morphological properties, as well as electrochemical behavior of the prepared materials as anodes for LIBs are reported. An *in*-operando X-ray diffraction and ex-situ X-ray photoelectron spectroscopy were carried out with the aim of understanding the structural changes and the reaction mechanism during cycling.

2. Experimental section

2.1. Synthesis process

$Ni_{1.5}V_2(PO_4)_3$/C (NVP/C) and $Mn_{1.5}V_2(PO_4)_3$/C (MVP/C) were prepared via the sol-gel synthesis method. The solution was obtained by dissolving in deionized water and phosphoric acid H_3PO_4 (Sigma-Aldrich, ≥85 %), stoichiometric amounts of ammonium metavanadate NH_4VO_3 (Sigma-Aldrich, 99 %) along with nickel (II) acetate tetrahydrate $Ni(CH_3COO)_4{\cdot}4H_2O$ (Sigma-Aldrich, 98 %) for NVP/C or manganese (II) acetate tetrahydrate $Mn(CH_3COO)_4{\cdot}4H_2O$ (Sigma-Aldrich, 98 %) for MVP/C. During the synthesis, citric acid was added with a molar ratio of 2 to 1 citric acid to the final product, as an in-situ carbon coating agent and to ensure chelation and reduction of vanadium. The solution was heated in an oil bath at 80 °C to form the gel, which was later dried at 100 °C overnight. The obtained product was ground in an agate mortar and thermally treated at 800 °C for 10 h under argon flow with a heating rate of 2 °C.min ^{1}.

2.2. Materials characterization

The thermogravimetric analysis was conducted via LABSYS evo to determine the adequate thermal treatment temperature for the synthesis of the samples and to evaluate occurring chemical or compositional changes. The analysis was performed under argon flow with a ramp of 5 °C.min ^{1}. An additional TGA was conducted under air for the synthesized materials with a ramp of 5 °C.min ^{1} in order to deduce the carbon content.

X-ray diffraction (XRD) was carried out using a Bruker D8 diffractometer with Cu-Kα radiation (α1 = 1.54056 Å). The XRD patterns were collected between 10° and 65° (2θ) with a step size of 1°/min. The morphologies and size distributions of the synthesized materials were inspected using high-resolution scanning electron microscopy (HR-SEM) in a Zeiss Gemini500-Field emission. To obtain a surface-sensitive imaging at nanoscale resolution, images were recorded at low voltage (1 kV) with an in-lens secondary electron detector. Raman Spectroscopy was performed using a LabRAM HR Evolution Raman spectrometer (HORIBA Scientific).

Nitrogen adsorption measurements were performed using the guest-free (evacuated) samples on 3-Flex Surface Characterization Analyzer (Micromeritics) at pressures up to 1 bar. In a typical experiment, about 60 mg of each sample was transferred (dry) to a glass sample cell and firstly evacuated at room temperature using a turbo molecular vacuum pump and then gradually heated to 160 °C at a rate of 5 °C.min ^{1}, held for 6 h and cooled to room temperature. The cryogenic temperatures for the nitrogen sorption measurements were controlled using liquid nitrogen baths at 77 K. The apparent surface areas were determined from the nitrogen adsorption isotherms collected at 77 K by applying the Brunauer-Emmett-Teller (BET) model. Pore size distribution analysis was performed using a BJH adsorption model system.

In operando measurements were recorded using a setup developed at the KIT in close cooperation with the STOE & Cie GmbH [15,16]. The diffractometer uses an Ag-source (E = 22.123 keV, λ = 0.55942 Å) with a focusing Ge 111 monochromator. A Dectris MYTHEN 2 2K double detector with a fixed distance between both detectors of little less than the width of a module (approximately 18°of 2θ) is mounted at a radius of 130 mm from the central axis of the goniometer. The diffraction patterns were performed in the 2θ range of 0 to 36°, with the effective angular resolution of 0.015° with the acquisition time of 20 min per pattern.

The electrochemical cells used for the *in* operando XRD measurements consist of a 2032-type coin cell with a Kapton window (125 mkm thickness of the Kapton film) for the beam entrance. The electrochemical tests within *in* operando cells were accomplished using a galvanostatic system μAUTOLAB-FRA2, TYPE III controlled by NOVA.

X-ray photoelectron spectroscopy (XPS) analysis was carried out via Escalab 250 Xi spectrometer, with Al Kα radiation (hν = 1486.6 eV). The tested electrodes were put on a sample holder with uPVC insulation tape (3 M part number 655) and transferred to an Ar-filled glove box connected to the spectrometer, to protect the samples from air and moisture. The analysis was done employing a standard charge compensation mode and an elliptic 325 × 650 μm X-ray beam spot. The core spectra were recorded with a pass energy of 20 eV, noting that the step size was 0.15 eV and iterative scans at a dwell time was 500 ms. The binding energy scale was calibrated from both NVP/C and MVP/C oxygen peak at 530.0 eV because of the solid electrolyte interface (SEI) formation which impacts the binding energy of carbon contamination peak.

2.3. Electrode preparation and electrochemical measurements

To prepare the electrode materials, the slurries were formulated by mixing 75 % of active material to 15 % of carbon black (Super P) to enhance the electronic conductivity and 10 % of the binder Poly-Vinylidene Fluoride (PVDF). The films were prepared by adding *N*-methyl-2-pyrolidone (NMP) (Sigma-Aldrich, ≥99.0) to the powder, spreading the suspension on copper foil which was later left to dry at 100 °C for 8 h was used as a solvent. The electrodes were cut via a precision perforator with a diameter of 12.7 mm and vacuumed at 120 °C for 12 h before transferring them to an Ar-filled glove box in order to assemble them in coin cells. The loading mass was around 3 mg. The CR2032 coin cells consisted of the electrode material against

metallic lithium, while $LiPF_6$ dissolved in (1 M) EC: EMC (50:50 by volume) served as the electrolyte. The cycling tests of the assembled coin cells were carried out on a BioLogic MPG2 battery cycler at room temperature, within the potential range 0.1–3.2 V and at various C-rates. Cyclic voltammetry tests were recorded within the same potential range and with a scan rate of 0.1 mV.s ^{1}.

3. Results and discussion

3.1. Thermal characterization

During the synthesis, both materials NVP/C and MVP/C unveiled that optimized conditions of thermal treatment are required. Thus, TGA/DTA measurements were conducted to determine an adequate temperature of phase formation.

The TGA curves shown in Fig. S1.a and b, traces the compositional changes occurring during thermal treatment for the NVP/C and MVP/C, respectively. The curves were recorded under argon flow in a temperature range between 50 and 900 °C at 5 °C.min ^{1}. For NVP/C material, three stages of weight loss are observed in temperature ranges of 50–200 °C, 200–800 °C, and 800–900 °C, while or MVP/C material, only two stages of weight loss are detected in temperature ranges of 50–200 °C and 200–800 °C. In both cases, the first weight loss, which is around 2.25 % for NVP/C and 1.91 % for MVP/C, could be attributed to the departure of adsorbed water and volatile organic compounds. The second significant weight loss, which is 32.03 % for NVP/C and 29.268 % for MVP/C, could be attributed to the decomposition of inorganic carbon present in acetates CH_3COO [17] as well as phase formation. An additional weight loss of about 8.928 % is observed for NVP/C material could be attributed to the decomposition of residual organic components and formation of intermediate phases.

The obtained results showed that both materials are largely stable until 800 °C. Thus, 800 °C is an adequate temperature for the thermal treatment of both materials.

According to TGA under air of the prepared materials, conducted between 30 and 900 °C at 5 °C.min ^{1}, and shown in Fig. S1.c and d, the

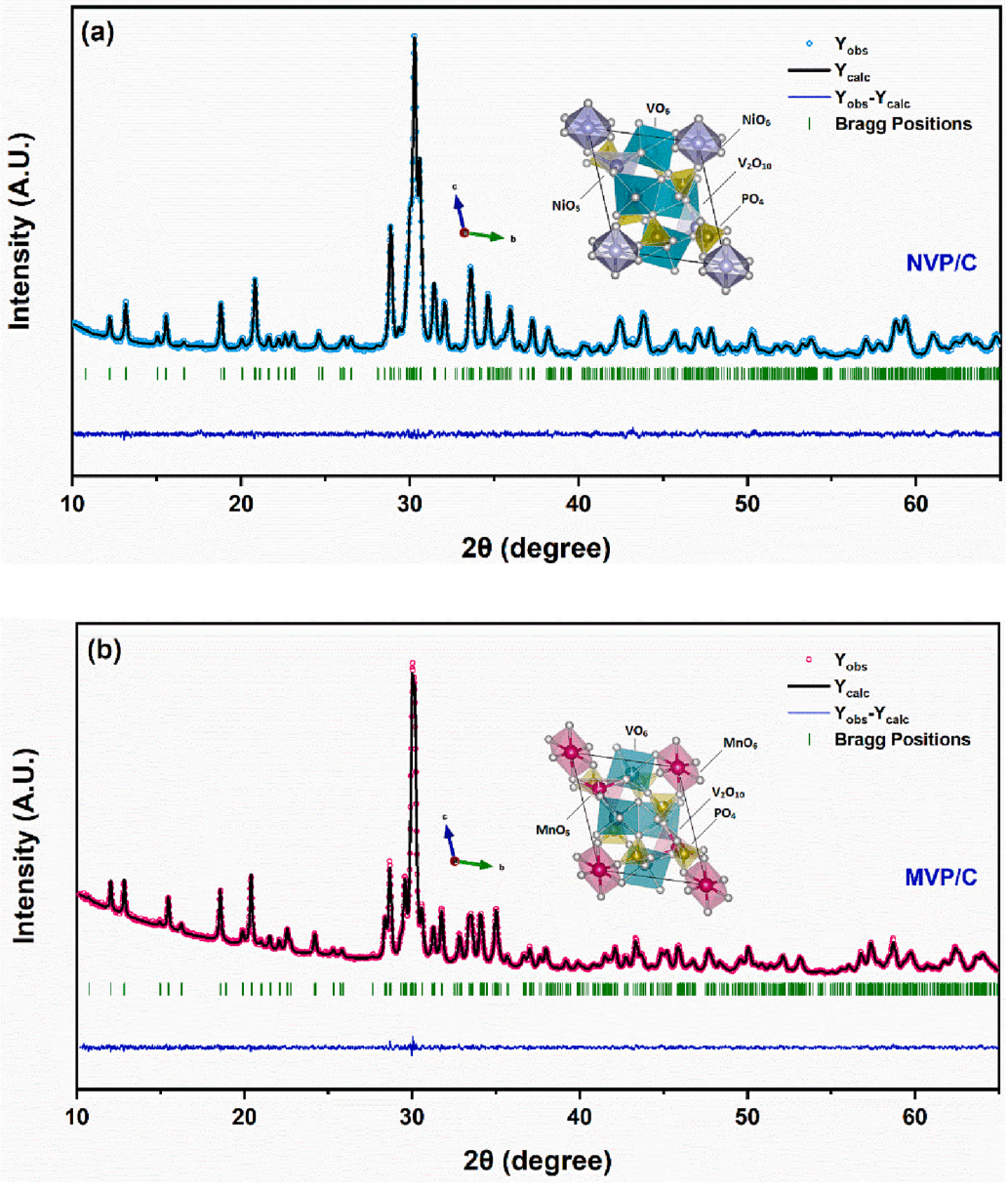

Fig. 1. Rietveld-refined XRD pattern of (a) NVP/C and (b) MVP/C. Vertical bars mark the calculated positions of the Bragg peaks of the product. Insets: Spatial projection (a) NVP/C and (b) MVP/C.

estimated carbon content is around ~6 % and ~4 % for NVP/C and MVP/C, respectively.

3.2. Crystal structure and morphology

The crystal structure and the purity of the prepared materials were examined by X-ray diffraction. Fig. 1.a and b depict the XRD patterns of NVP/C and MVP/C, respectively, as well as the spatial representations of their crystal structures. The patterns indicate that both samples show good crystallinity. Moreover, the absence of carbon peaks on both patterns reveals an amorphous character of the carbon existing in NVP/C and MVP/C materials.

Following a crystal structure refinement of NVP/C and MVP/C diffractograms using the Rietveld method and considering $Zn_{1.5}V_2(PO_4)_3$ (PDF 00-051-1630) as a starting structural model, the diffraction peaks of both patterns can be indexed based on a triclinic structure with space group *P*1 [18]. No impurity was detected. The unit cell parameters and atomic coordinates of NVP/C and MVP/C are displayed in Tables S1 and S3, respectively. Overall, the resulting crystallographic values calculated by applying Rietveld refinement are in agreement with those of Zn-based [18] and Fe-based [12] NaSICon materials. The MVP/C lattice parameters are higher than NVP/C ones which is expected as Mn^{2+} radius is bigger than Ni^{2+}.

The structure consists of two types of dioctahedral edge-sharing V_2O_{10} groups linked via PO_4 tetrahedra forming a tridimensional framework $[V_4P_6O_{24}]_\infty$. The metal cation M(1) (M = Ni, Mn) is located in the center of the tunnel formed by the tridimensional framework $[V_4P_6O_{24}]_\infty$. Consequently, distorted MO_6 octahedra (M = Ni, Mn) are formed. Moreover, the second metal M(2) (M = Ni, Mn) occupies the border of the tunnel and forms a severely distorted trigonal bipyramid MO_5 (M = Ni, Mn). Tables S2 and S4 display the most important metal-oxygen distances in polyhedra forming the structure for NVP/C and MVP/C materials. With the ionic radii of involved ions taken into consideration, the obtained values from structure refinement are in agreement with the reported ones in literature [12,18] confirming the accuracy of the structural model.

Raman spectra of NVP/C and MVP/C, plotted in Fig. S2, shows stretching (ν_1 and ν_3) and bending (ν_2 and ν_4) PO_4 modes typically reported for NaSICon phosphates [19]. The symmetric non degenerate PO stretching modes, the antisymmetric doubly degenerate PO stretching modes, the triply degenerate OPO bending modes, as well as the triply degenerate antisymmetric and harmonic OPO bending modes are all present for both materials [19]. Also, the presence of residual carbon resulting from the in-situ carbon coating of the materials via citric acid was confirmed. The two typical D- and G-bands, characteristic of carbon are detected around 1325 cm^{-1} and 1595 cm^{-1}, for NVP/C, and 1336 cm^{-1} and 1600 cm^{-1} for MVP/C. The additional bands appearing around 1400 cm^{-1} and 1368 cm^{-1} for NVP/C and MVP/C, respectively are attributed to disordered carbon films [20,21]. The bands around 1532 cm^{-1} 1508 cm^{-1} for NVP/C and MVP/C, respectively, are attributed to the sp^2 bonded carbon (D″ band).

The morphologies of NVP/C and MVP/C powders were analyzed by scanning electron microscopy (SEM). Fig. S3 illustrates the obtained micrographs. The powders particles are relatively micrometric with defined edges and non-homogeneous size distribution. Also, the micrographs show the presence of pores, beneficial for the electrolyte penetration and Li ions diffusion. This porosity is later confirmed and evaluated by BET analysis.

The N_2 sorption isotherms recorded at 77 K (Fig. S4.a and b) showed that NVP/C and MVP/C exhibit fully reversible Type-V isotherm with low energy of adsorption at low relative pressures, a characteristic of mesoporous materials. The isotherms also contain hysteresis loops at higher relative pressures (P/P_0) which is indicative the presence of mesoporosity within the structures of the prepared materials. The Brunauer-Emmett-Teller (BET) model was employed to determine the specific surface areas of the NVP/C and MVP/C materials. The BET surface areas are about 18.5 $m^2.g^{-1}$ and 7.5 $m^2.g^{-1}$ for NVP/C and MVP/C, respectively. The pore size distributions (PSDs) for NVP/C and MVP/C were also assessed from the nitrogen adsorption data using BJH model (insets in Fig. S4.a and b) and revealed the presence of pores with non-homogeneous pore shape distribution. Moreover, the dominant broad peaks of the PSDs appear in the 5–50 nm range confirming the mesoporous character of the prepared materials. The PSD analyses also evidenced the presence of some macropores within the structures of the prepared materials with average pore diameters centered around 70 nm. It is worth mentioning that this porosity could contribute to the capacity [22] as it facilitates the electrolyte infiltration and thus the active material-electrolyte contact [23].

3.3. Electrochemical performance

The electrochemical tests were carried out on NVP/C and MVP/C as negative electrodes versus Li^+/Li within a potential range of 0.1–3.2 V. The current densities at 1C are around 336 $mA.g^{-1}$ and 343 $mA.g^{-1}$ for NVP/C and MVP/C, respectively. Fig. 2.a and b show the electrochemical behavior of NVP/C and MVP/C anodes, respectively, at 0.2C rate during the first twenty-five discharge-charge cycles. Regarding NVP/C material, a high initial discharge capacity is delivered by a Li//NVP/C electrochemical cell reaching 880 $mAh.g^{-1}$. However, the reversible charge capacity is around 495 $mAh.g^{-1}$. This major capacity loss is only remarkable in the first discharge-charge cycle as the performance gradually stabilizes for the subsequent cycles.

Similarly, the initial discharge capacity delivered by Li//MVP/C is noticeably high and reaches 933 $mAh.g^{-1}$, then drops to 537 $mAh.g^{-1}$ in the second discharge-charge cycle. The initial irreversible capacity loss decreases significantly for the subsequent cycles, and by the twenty fifth charge, a reversible charge capacity of 400 $mAh.g^{-1}$ is delivered. It is worth noting that the charge capacity fading is less pronounced in the case of MVP/C compared to NVP/C, as MVP/C is more structurally stable than NVP/C.

Furthermore, the initial discharge profiles of the studied materials show two plateaus for NVP/C at 1.5 V and 0.10 V, and two for MVP/C at 1.5 V and 0.21 V. Also, slopes at about 1 V, 0.75 V, 0.51 V. The charge profiles of NVP/C exhibit two plateaus around 0.5 V and 1.7 V, while the charge profiles of MVP/C show similar ones around 0.46 V and 1.75 V. Those reversible plateaus could be attributed to a sequence of phase transition process [24].

For both anode materials, the loss in the initial discharge capacities is linked to the SEI formation, which inhibits the electrolyte penetration as well as structural changes. In Fig. 2.a and b, the shapes of discharge-charge profiles change during the first charge implying a conversion reaction upon lithiation-delithiation. This reaction mechanism is confirmed by cyclic voltammetry and validated by X-ray photoelectron spectroscopy as well as in-situ operando diffraction of synchrotron radiation.

The cyclic voltammograms (CV) of NVP/C and MVP/C are displayed in Figs. 2.c and d, respectively. During the first discharge, four cathodic peaks appear around 1.1, 0.78, 0.5, and 0.1 V for NVP/C and three peaks at about 1.32, 0.66, 0.21 V for MVP/C, in addition to a sloping curve down to 0.1 V for both materials. This may be explained by the formation of new by-products. The peaks below 1.0 V, could be assigned to the formation of species issued from the conversion reaction and the formation of SEI along with the electrolyte side reactions [7]. Further, the Li^+ insertion into amorphous carbon could also contribute to the broad peak around 0.1 V. By the same token, starting from the first charge, the CV profiles show two reversible anodic peaks, barely noticeable for NVP/C around 1.0 and 2.3 V and two anodic peaks for MVP/C at about 0.9 and 2.2 V. The corresponding cathodic peaks show at 0.8 and 1.68 V for NVP/C, and at 0.96 and 1.92 V for MVP/C. Those peaks are attributed to the oxidation and reduction of present transition metals (V, Ni and Mn) [22].

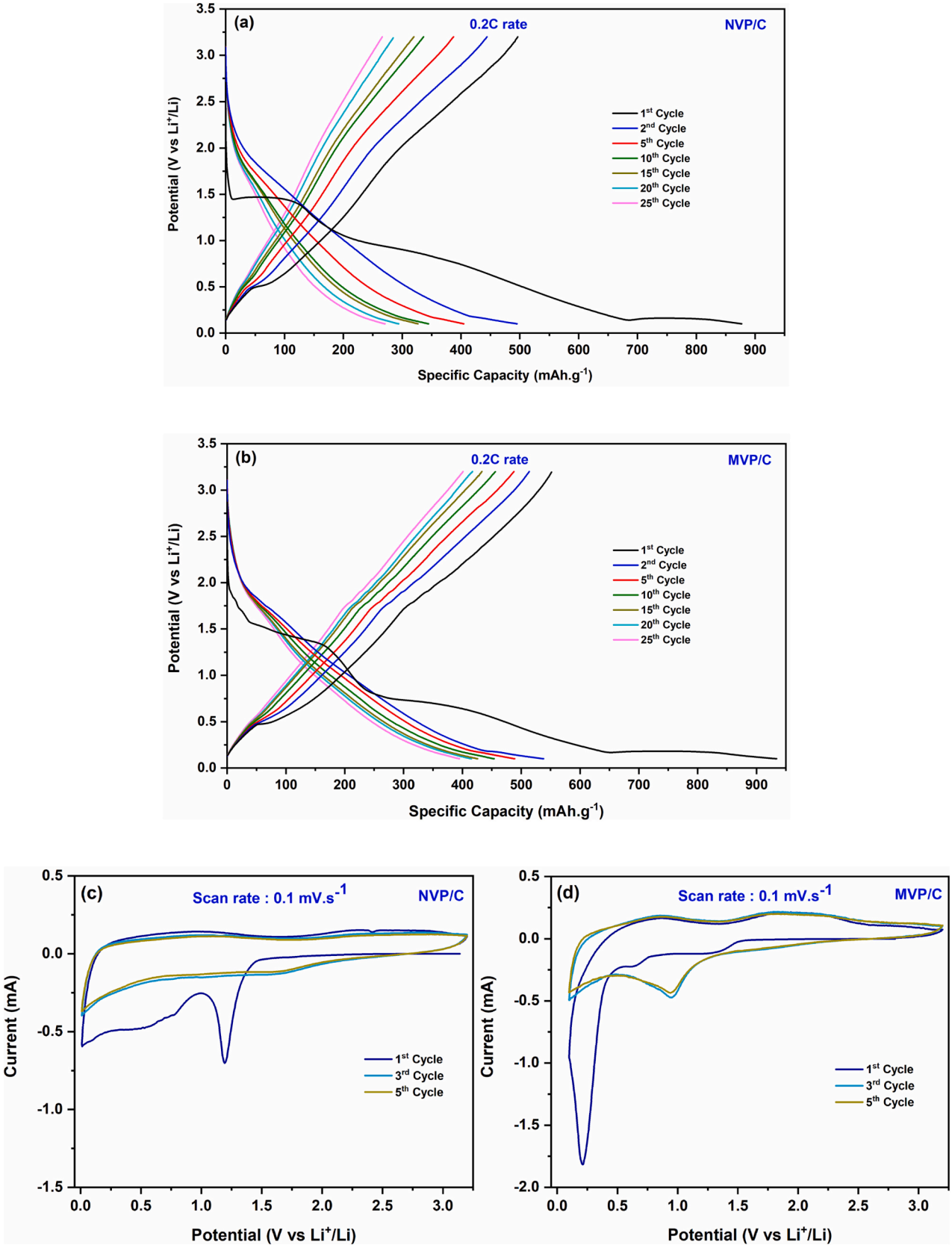

Fig. 2. The electrochemical discharge/charge profile in the potential range 0.1–3.2 V at 0.2C rate of (a) NVP/C and (b) MVP/C, Cyclic voltammetry test at 0.1 mV s^{-1} scan rate of (c) NVP/C and (d) MVP/C.

Furthermore, to evaluate the long-term cycling durability and stability of the anode materials NVP/C and MVP/C, the corresponding half-cells were cycled at two fast rates 2C and 5C for 1000 cycles, and the results are given in Fig. 3.a and b, respectively. For the first 100 cycles, in the case of NVP/C (inset of Fig. 3.a), the discharge capacity of the material is relatively higher at 5C rate, mainly due to electrochemical kinetics [7]. The capacities of the material in the second cycle, at 2C and 5C rates are 312 mAh.g ^{1} and 368 mAh.g ^{1}, respectively. These capacities decline by the 100th cycle to nearly 80 mAh.g ^{1}. The material manages to keep the obtained capacity reversible for the subsequent 900 cycles. The MVP/C anode material exhibits a relatively identical behavior to NVP/C. Although the capacity declines from around 290 mAh.g ^{1} in the second cycle to 82 mAh.g ^{1} in the 100th cycle, the material shows an improved and more stable performance under 2C rate for the first 100 discharge-charge cycles (inset of Fig. 3.b). Further cycling reveals another capacity drop around the 700th cycle at faster rate 5C, from 70 mAh.g ^{1} to 40 mAh.g ^{1}. It is important to note that the decay of the capacity upon cycling result mainly from the continuous consumption of the active material during the conversion mechanism. This conversion mechanism depends on the rate, the nature of the transition metal and also on the electrolyte especially when a very low cut-off voltage is used. This decomposition results on species, generally nanocomposites, that cannot react with the inserted lithium to form new alloys and thus increasing the capacity. Only a capacitive behavior governs the mechanism for long term cycles where the formed nanocomposite continuous to store lithium without any electrochemical reaction. To confirm this capacitive behavior, we conducted a multi-rate CV study of the studied electrode materials.

Cyclic voltammetry tests of NVP/C and MVP/C at scan rates from 0.2 mV.s ^{1} to 0.45 mV.s ^{1} are depicted in Fig. S5. At 0.2 mV.s ^{1}, cathodic peaks are observed around 0.97 V and 0.93 V for NVP/C and MVP/C, respectively. The increase on scan rate leads to the disappearance of the cathodic peak in the case of NVP/C while it gets broader in the case of MVP/C. While no anodic peaks are shown for NVP/C, two anodic peaks are detected for MVP/C at 1.1 V and 2.26 V. Moreover, the shape of the CV curves tends towards a quasi-rectangular shape, which indicates a capacitive contribution to the electrochemical process [25].

The differential capacity profiles (dQ/dV) of the first and fifth cycles of NVP/C and MVP/C, exhibited in Fig. S6, confirm a pseudocapacitive storage contribution starting from first charge for both materials, but

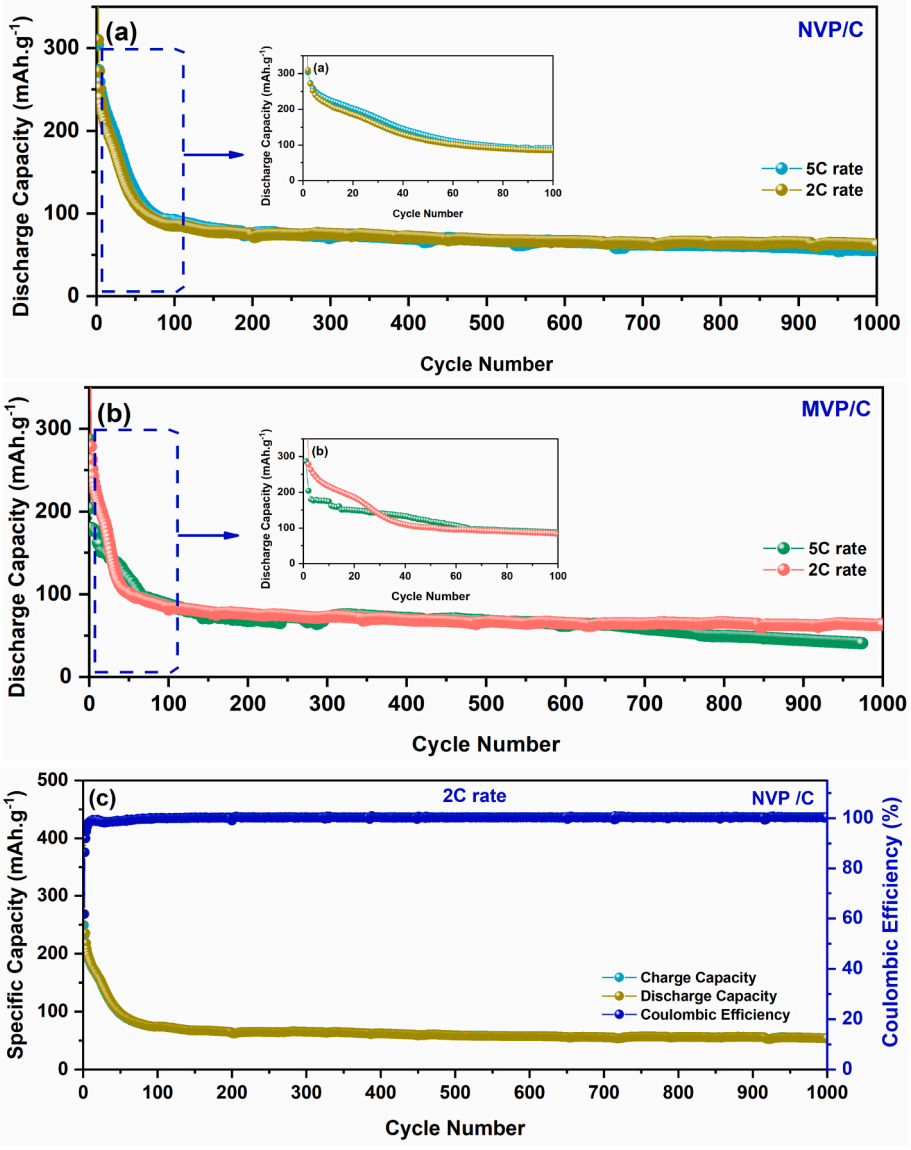

Fig. 3. Discharge capacity vs. cycle number at 2C rate and 5C rate for (a) NVP/C and (b) MVP/C, Specific capacity, and coulombic efficiency at 5C-rate for 1000 cycles for (c) NVP/C and (d) MVP/C, Rate capability at multiple C-rates of (e) NVP/C and (f) MVP/C.

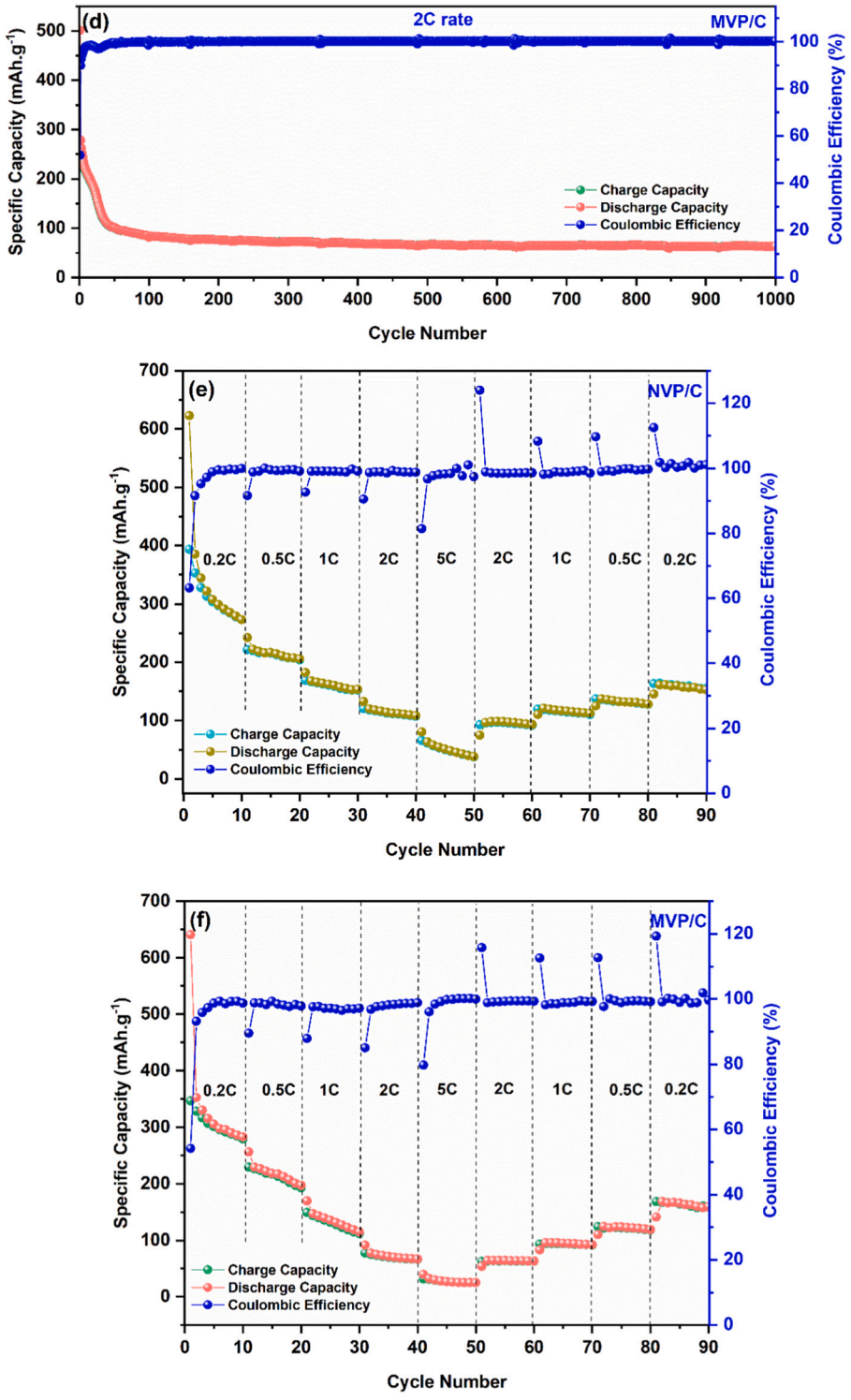

Fig. 3. (*continued*).

more emphasized in the case of MVP/C. This pseudocapacitive contribution is linked to the occurring phase changes and stresses on crystal structures of the materials following Li ion insertion, which triggers capacity fade and influences both materials cyclability [26].

Moreover, as depicted by Fig. 3.c and d, for the first 100 cycles both materials show a good coulombic efficiency with the lowest values being around 97 % for NVP/C and 95 % for MVP/C. In the subsequent 900 cycles, good capacity retentions are observed, which were about 76 % for NVP/C and 74 % for MVP/C. For the first 2 cycles, the coulombic efficiencies of the materials are lower than 90 %, however, they increase afterwards and stabilize around 99.9 % until the 1000nd cycle.

The rate performances of NVP/C and MVP/C are represented in Fig. 3.e and f, respectively. The rate capability tests were carried out at incremental C-rates from 0.2C to 5C and back, with ten discharge-charge cycles for each C-rate. Without taking into consideration the first discharge-charge cycle, a specific capacity of nearly 400 mAh.g ^{1} at 0.2C is noticed at the second cycle for NVP/C and 360 mAh.g ^{1} for MVP/C. However, those specific capacities decline by the 10th cycle

reaching 272 mAh.g ^{1} and 282 mAh.g ^{1} for NVP/C and MVP/C, respectively. The detected significant capacity loss for both materials is due to phenomena including SEI formation and side reactions resulting in the appearance of new phases (such electrolyte decomposition to LiF, $Li_xPF_yO_z$, etc.) evidenced by X-ray photoelectron spectroscopy, or irreversible structural changes which were later confirmed by in-operando measurements. Further, following the de-lithiation, the Jahn-Teller distortion, generated by the unstable octahedrally coordinated Ni^{3+} and Mn^{3+} of MO_6 (M = Ni, Mn), could likely contribute to the instability during cycling [27]. Over and above, increasing C-rates could contribute to a mild capacity decay as observed on Fig. 3.e and f. Later, the specific capacities increased when decreasing C-rates, and approximate specific capacities of 160 mAh.g ^{1} and 152 mAh.g ^{1} were maintained reversible at 0.2C for NVP/C and MVP/C, respectively.

3.4. *In-operando X-ray diffraction*

In-operando X-ray diffraction was used to detect the changes occurring on the crystal structure of the studied anode materials NVP/C and MVP/C, during the first discharge-charge cycles at 0.2C rate in a potential range of 0.1–3.2 V. The series of selected patterns are shown in Fig. 4. To begin with, all the peaks of $M_{1.5}V_2(PO_4)_3$/C (M = Ni, Mn) are ascribed to the triclinic structure with *P*T space group in agreement with the refined crystal structure presented before. Besides, sharp intense peaks related to strong copper reflections were detected for NVP/C and MVP/C.

As illustrated in Fig. 4a, the NVP/C patterns show two main reflections at OCV located at 6.5° and 10.95° of 2θ corresponding to 111 and 021, respectively. Both reflections show a slight shift towards low two-theta angles simultaneously with the Li^+ insertion indicating changes in the lattice parameters. The 111 reflection stands during the charge where its intensity decreases gradually until it disappears. However, the 021 reflection shows a significant broadening during Li^+ insertion and disappears by the end of discharge.

For MVP/C, three reflections can be recognized which are 111, 1–11 and 021 situated at 6.5°, 7.55° and 10.95° of 2θ, respectively. All over the discharge, the reflection 111 changes its position towards lower two-theta angles while the new detected reflection 1–11 and the 021 reflection exhibit a clear peak broadening and weakening of intensity, tending to disappear. In the subsequent charge, the patterns conserved the same peaks with differences mainly in intensities.

It can be concluded that the crystallinity of the materials degrades throughout the first discharge-charge process. Both materials exhibit signs of amorphization of structure comprising the disappearance of some peaks during the intercalation-deintercalation of Li ions. The shifts of peaks towards low two-theta angles are indicative of slight expansions of lattices for both materials. Such irreversible structural changes are suggested to impact the electrochemical reversibility, thus leading to undesirable performances during cycling.

3.5. *Ex-situ X-ray photoelectron spectroscopy*

The ex-situ X-ray photoelectron spectroscopy (XPS) technique was performed to verify the electrode/electrolyte interactions by investigating the elemental compositions, and the growth of SEI, built on the surfaces of the electrodes of NVP/C and MVP/C and thus impacting their electrochemical performance. The NVP/C and MVP/C pristine electrodes (before cycling) consisted of Cu-foil on which the slurry is deposited and were analyzed before cycling. The electrolyte used for cycling involved $LiPF_6$ salt dissolved in (1 M) EC: EMC (50:50 by volume). Following the cycling of the anode materials at 1C rate, the electrodes were recovered after the first discharge, the first charge, the fifth discharge-charge cycle, and the 20th discharge-charge cycle. Figs. 5 and 6 illustrate the deconvoluted spectra of F 1s (a_1–a_5), O 1s (b_1–b_5), C 1s (c_1–c_5) and P 2p (d_1–d_5) core levels of NVP/C and MVP/C, respectively at the five different states mentioned previously. The parameters used for the fitting as well as the binding energies are reported in Table S5.1–5 for NVP/C and Table S6.1–5 for MVP/C.

Before cycling, the deconvoluted spectra of F 1s showed the presence of semi-ionic C—F at 687.0 eV for NVP/C and covalent C—F at 687.9 eV for NVP/C while only covalent C—F was observed for MVP/C at 688.4 eV [28]. The O 1s spectra showed the presence of an oxygen lattice (O^2) or transition metal (V, Ni)-oxygen peak at 530.9 eV for NVP/C [29]. This peak was not observed for MVP/C sample most likely due to dominance of other oxygenated deposited species and/or the disproportionation reaction of Mn on the surface of the electrode with Mn^{2+} dissolution into electrolyte [30]. Furthermore, a peak showing at 532.2 eV for NVP/C and 533.6 eV for MVP/C is related to P═O [31] and/or Li_2CO_3 [29]. In the case of MVP/C, the peak around 534.0 eV is attributed to C-O-C [32].

As for C 1s, the spectra of both anodes reveal the presence of residual carbon, carbon black through the dominating bonds of C═C [32] and C—C [33], which are indicative of graphitization, as well as C—H [33] C═O, O-C-O [33]. The presence of PVDF, on the surface of the electrodes before proceeding to cycling, is evidenced through CH_2 peak around ~286 eV [34] and CF_2 peak around ~290 eV [35,36]. The P 2p spectra, corresponding to the phosphorus contained in NVP/C and MVP/C, is deconvoluted to $(PO_4)^3$ at ~133 eV [37] and P—O (P $2p_{3/2}$) at ~134.0

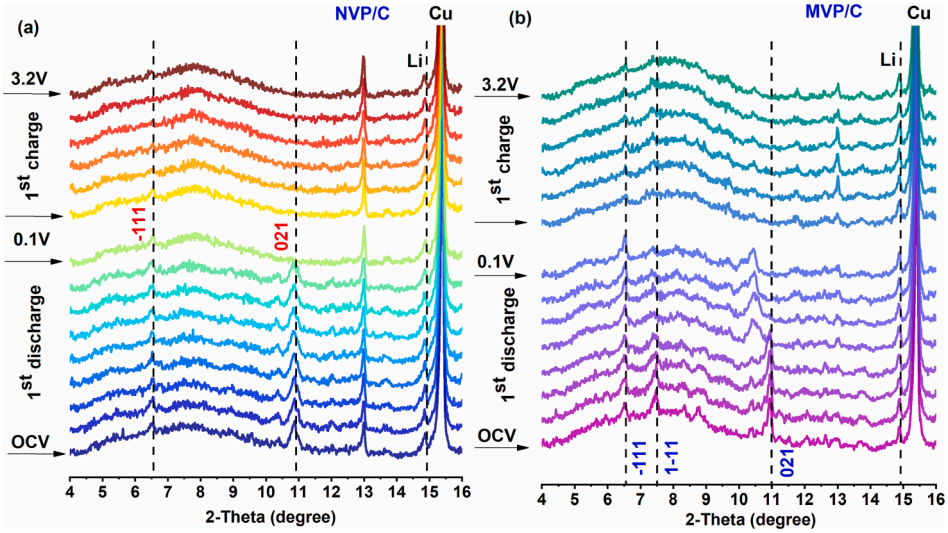

Fig. 4. Operando diffraction patterns during the first discharge-charge in a potential range 0.1–3.2 V at 0.2C rate for (a) NVP/C and (b) MVP/C.

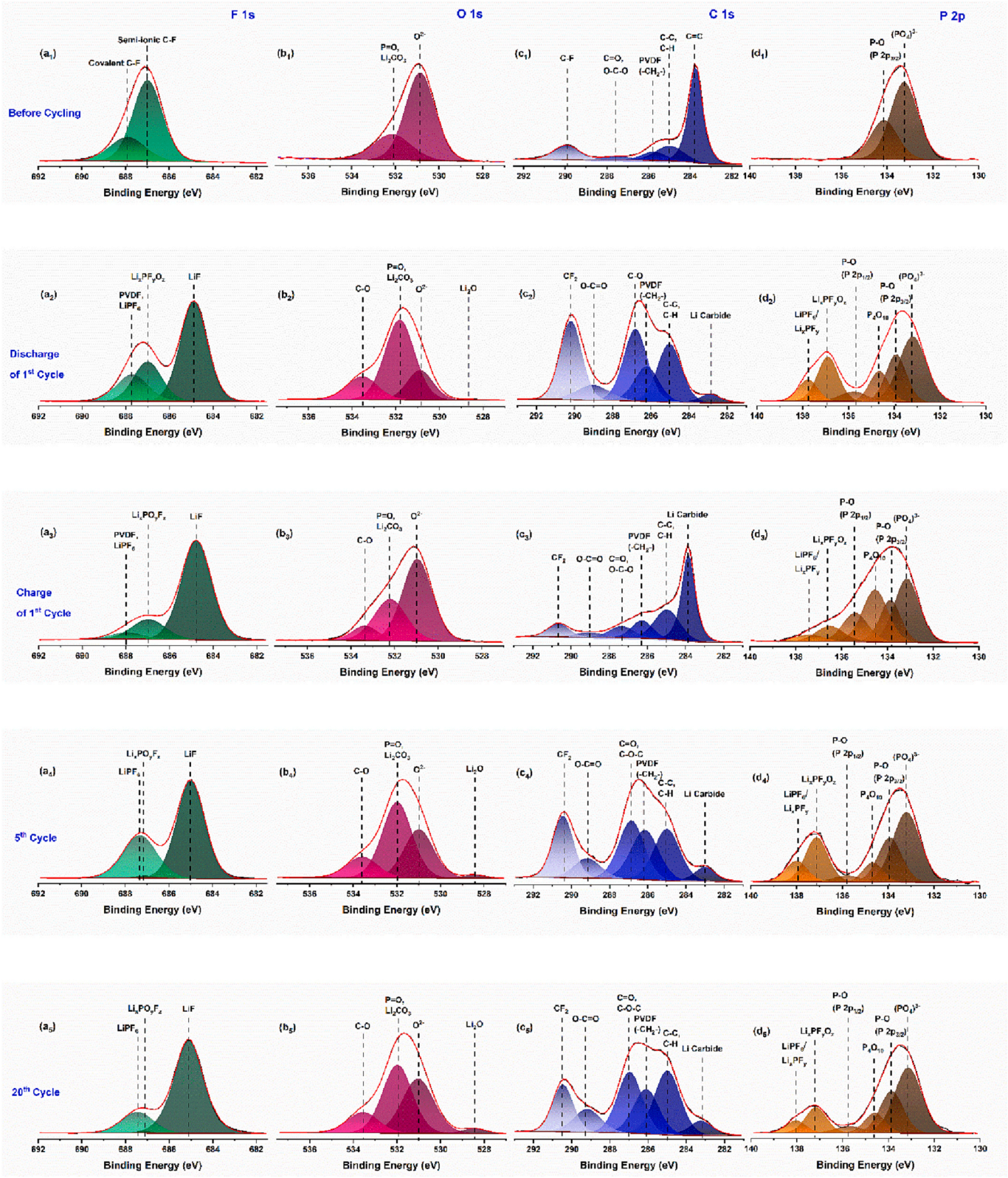

Fig. 5. XPS core spectra in the (a_1–a_5) F 1s, (b_1–b_5) O 1s, (c_1–c_5) C 1s, and (d_1–d_5) P 2p regions, collected of NVP/C anode material at different cycling stages.

eV [36], as shown in Fig. 5-d_4 and d_4.

After the first discharge, it is found for both anode materials, that the F 1s peak reveals the presence of new components through three new peaks. The first peak showing around 685.0 eV for NVP/C and 686.0 eV for MVP/C is attributed to LiF [33,38]. The second peak appearing around 687.0 eV for NVP/C and 687.5 eV for MVP/C can be related to $Li_xPF_yO_z$ [33] and/or P—F [39], while the last peak at 687.7 eV for NVP/C and 688.7 eV for MVP/C is associated to and $LiPF_6$ [39] and/or PVDF [33]. The new bonds are definitely resulting from electrolyte decomposition. In the following discharge-charge cycles the intensity of the

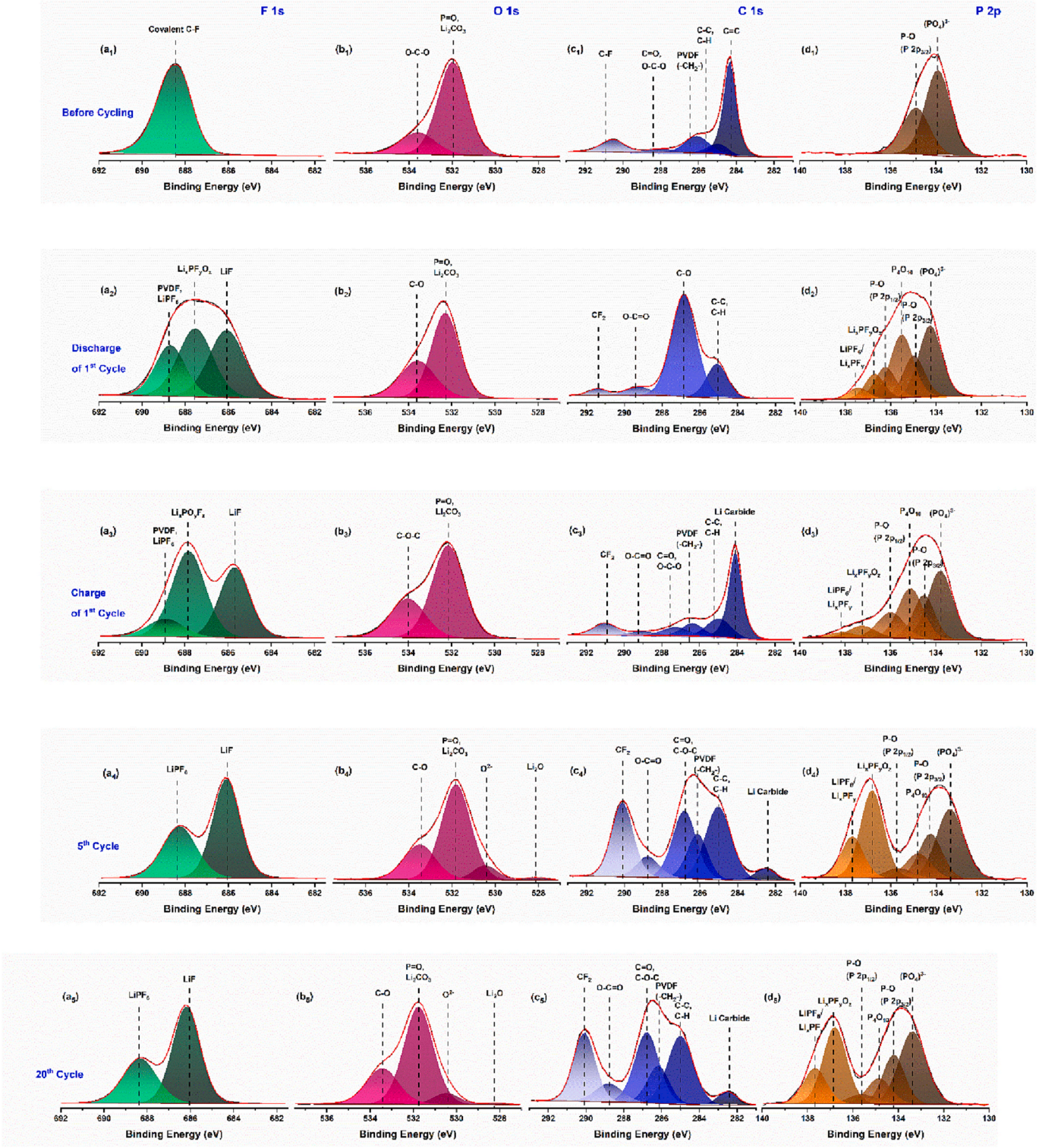

Fig. 6. XPS core spectra in the (a_1–a_5) F 1s, (b_1–b_5) O 1s, (c_1–c_5) C 1s, and (d_1–d_5) P 2p regions, collected of MVP/C anode material at different cycling stages.

$Li_xPF_yO_z$ bond clearly decreases for both materials until disappearance. By the 20th cycle, only two bonds LiF and $LiPF_6$ were still obvious, although their intensities varied suggesting a regression in electrolyte decomposition.

For NVP/C, and in addition to the bonds revealed before cycling, the deconvolution of O 1s spectra shows the presence of two additional peaks which are Li_2O [37] at 528.7 eV and C—O [33] 533.5 eV. The two peaks could be related to components resulting from the decomposition of electrolyte. However, in the case of MVP/C, no further bonds were observed on the O1s deconvoluted spectrum, and the revealed peaks were identical to those noticed before cycling. This can be indicative of a higher stability of oxygen in the case of MVP/C sample compared to NVP/C sample. The new components attributed to electrolyte decomposition were noticeable by the fifth cycle for MVP/C.

Similarly, the C1s fitted spectrum of NVP/C after the first discharge, shows a new component around 282.9 eV which is Li carbide (Li_2C_2)

[40]. This bond was noticeable after the first charge for MVP/C. Also, the presence of an additional O-C=O is remarked [31,41]. By the end of the fifth discharge-charge cycle, all the bonds were kept unchanged and identical to those reported on the 20th discharge-charge cycle.

The P 2p spectra of NVP/C and MVP/C following the first discharge, showed the rise of new peaks, ascribed to components generated from electrolyte interactions namely, P_4O_{10} (P^{+5}) [42], P—O (P $2p_{1/2}$) [35,36], $Li_xPF_yO_z$ [33], Li_xPF_y [36,43] and $LiPF_6$ [38,43]. By the fifth discharge-charge cycle, the intensities of the peaks $(PO_4)^3$ and P—O (P $2p_{3/2}$) were stable while those of Li_xPF_yO, Li_xPF and $LiPF_6$ tended to increase.

4. Conclusion

This work introduces two NaSICon-structured materials $M_{1.5}V_2(PO_4)_3/C$ (M = Ni, Mn) as anodes for Li-ion batteries. The samples were prepared via sol-gel synthesis technique and the thermal treatment was at 800 °C under argon flow. It was demonstrated that the materials crystallize in a distorted triclinic structure with a $P\bar{1}$ space group. Raman spectroscopy confirmed the structure through the presence of bands related to stretching and bending modes of PO_4, PO and OPO. Also, it evidenced the success of in situ carbon coating targeted during synthesis. The particles size of prepared NVP/C and MVP/C is micrometric as shown via SEM. The porosity of both materials was investigated by nitrogen sorption at cryogenic conditions. The electrochemical behavior of NVP/C and MVP/C, as anode materials, was examined in a voltage range of 0.1–3.2 V. The NVP/C anode delivered an initial discharge capacity of 880 mAh.g ^{1} while MVP/C delivered an initial discharge capacity of 993 mAh.g ^{1}. By the following charge, the specific capacities of NVP/C and MVP/C dropped to 495 mAh.g ^{1} 550 mAh.g ^{1}, respectively. Despite the initial irreversible capacity loss, the anode materials demonstrated good performance at high C-rates and long-term cycling stability as well as a high coulombic efficiency (~99.9). The effect of SEI formation on the electrochemical behavior, was investigated and later confirmed by operando diffraction of synchrotron radiations and ex-situ X-ray photoelectron spectroscopy.

CRediT authorship contribution statement

Mohja AMOU: Analysis & Data collection & Writing - original draft.
Badre LARHRIB: Formal analysis.
Noha SABI: Formal analysis & Writing - review & Investigations.
Mohammed SROUT: Data collection & Review & editing.
Ayalew H. ASSEN: Formal analysis & Writing - review.
Mohammed MANSORI: Formal analysis.
Oleksandr DOLOTKO: Writing - review & Investigations.
Nouredine OUELDNA: Formal analysis & Writing - review.
Hervé MARTINEZ: Writing - review & Investigations.
Ismael SAADOUNE: Funding acquisition & Supervision & Validation & Review & Editing.

Declaration of competing interest

The authors declare the following financial interests/personal relationships which may be considered as potential competing interests: Ismael SAADOUNE reports financial support was provided by OCP Foundation.

Data availability

No data was used for the research described in the article.

Acknowledgements

The authors are grateful to OCP for the financial support through the programs APHOS and APRD (2016–2025).

References

[1] D. Larcher, J.M. Tarascon, Towards greener and more sustainable batteries for electrical energy storage, Nat. Chem. 7 (1) (Jan 2015) 19–29.
[2] Haiping Jia, Pengfei Gao, Jun Yang, Jiulin Wang, Yanna Nuli, Z. Yang, Novel Three-Dimensional Mesoporous Silicon for High Power Lithium-Ion Battery Anode Material, 2011.
[3] L. Hu, et al., CrPO4/C composite as a novel anode material for lithium-ion batteries, J. Power Sources 441 (2019).
[4] L. Hu, S. Zheng, Z. Chen, B. Huang, J. Yang, Q. Chen, 3D graphene modified sphere-like VPO4/C as a high-performance anode material for lithium-ion batteries, Electrochim. Acta 284 (2018) 609–617.
[5] C. Delmas, A. Nadiri, J.L. Soubeyroux, The nasicon-type titanium phosphates Ati2 (PO4)3 (A=Li, Na) as electrode materials, Solid State Ionics 28–30 (1988) 419–423.
[6] B. Lang, B. Ziebarth, C. Elsässer, Lithium ion conduction in LiTi2(PO4)3 and related compounds based on the NASICON structure: a first-principles study, Chem. Mater. 27 (14) (2015) 5040–5048.
[7] M. Srout, M. Amou, K.M. Fromm, I. Saadoune, On the Ni0.75Ti1.5Fe0.5(PO4)3/C NASICON-type electrode material, J. Electroanal. Chem. 880 (2021).
[8] J. Gaubicher, C. Wurm, G. Goward, C. Masquelier, L. Nazar, Rhombohedral form of Li3V2(PO4)3 as a cathode in Li-ion batteries, Chem. Mater. 12 (11) (2000) 3240–3242.
[9] C. Burba, R. Frech, Vibrational spectroscopic studies of monoclinic and rhombohedral Li3V2(PO4)3, Solid State Ionics 177 (39–40) (2007) 3445–3454.
[10] X.H. Rui, N. Yesibolati, C.H. Chen, Li3V2(PO4)3/C composite as an intercalation-type anode material for lithium-ion batteries, J. Power Sources 196 (4) (2011) 2279–2282.
[11] W.f. Mao, H.q. Tang, Z.y. Tang, J. Yan, Q. Xu, Configuration of Li-ion vanadium batteries: Li3V2(PO4)3(cathode) Li3V2(PO4)3(anode), ECS Electrochem. Lett. 2 (7) (2013) A69–A71.
[12] M. Amou, et al., Fe1.5V2(PO4)3/C phosphate as a negative electrode material for high-rate performance lithium-ion batteries, J. Power Sources 532 (2022).
[13] Y.J. Mai, J.P. Tu, C.D. Gu, X.L. Wang, Graphene anchored with nickel nanoparticles as a high-performance anode material for lithium ion batteries, J. Power Sources 209 (2012) 1–6.
[14] X. Ou, et al., Mn doped NaV3(PO4)3/C anode with high-rate and long cycle-life for sodium ion batteries, Energy Storage Mater. 12 (2018) 153–160.
[15] M. Herklotz, et al., A novel high-throughput setup for in situ powder diffraction on coin cell batteries, J. Appl. Crystallogr. 49 (1) (2016) 340–345.
[16] P. Sharma, et al., Synthesis and characterization of a multication doped Mn spinel, LiNi(0.3)Cu(0.1)Fe(0.2)Mn(1.4)O(4), as 5 V positive electrode material, ACS Omega 5 (36) (Sep 15 2020) 22861–22873.
[17] Yao Zhang, et al., Sacrificial template strategy toward a hollow LiNi1/3Co1/3Mn1/ 3O2 nanosphere cathode for advanced lithium-ion batteries, ACS Omega 2 (11) (Nov 30 2017) 7593–7599.
[18] S. Boudin, A. Grandin, A. Leclaire, M.M. Borel, B. Raveau, The original structure of Zn3V4(PO4)6 involving bioctahedral V2O10 units and ZnO5 trigonal bipyramids, J. Solid State Chem. 115 (1995) 140–145.
[19] A. Aatiq, A. Marchoud, H. Bellefqih, M.R. Tigha, Structural and Raman spectroscopic studies of the two M0.50SbFe(PO4)3 (M = Mg, Ni) NASICON phases, Powder Diffract. 32 (S1) (2017) S40–S51.
[20] R. Chen, R. Heinzmann, S. Mangold, V.S.K. Chakravadhanula, H. Hahn, S. Indris, Structural evolution of Li2Fe1-yMnySiO4 (y = 0, 0.2, 0.5, 1) cathode materials for Li-ion batteries upon electrochemical cycling, J. Phys. Chem. C 117 (2) (2013) 884–893.
[21] K. Zaghib, Magnetic studies of phospho-olivine electrodes in relation with their electrochemical performance in Li-ion batteries, Solid State Ionics 179 (1–6) (2008) 16–23.
[22] Q. Fu, et al., Electrochemical and structural investigation of calcium substituted monoclinic Li3V2(PO4)3 anode materials for Li-ion batteries, Adv. Energy Mater. 9 (33) (2019).
[23] X. Ma, et al., Tuning crystal structure and redox potential of NASICON-type cathodes for sodium-ion batteries, Nano Res. 13 (12) (2020) 3330–3337.
[24] X.H. Rui, N. Yesibolati, S.R. Li, C.C. Yuan, C.H. Chen, Determination of the chemical diffusion coefficient of Li+ in intercalation-type Li3V2(PO4)3 anode material, Solid State Ionics 187 (1) (2011) 58–63.
[25] N. Sabi, et al., Evidence of a pseudo-capacitive behavior combined with an insertion/extraction reaction upon cycling of the positive electrode material P2-NaxCo0.9Ti0.1O2 for sodium-ion batteries, ChemElectroChem 6 (3) (2019) 892–903.
[26] M.J. Sussman, A. Yasin, G.P. Demopoulos, On the complex interplay of crystallinity and surface area effects on Li-ion intercalation and pseudocapacitive storage properties of nanocrystalline anatase, J. Power Sources 272 (2014) 58–67.
[27] C. Xu, et al., A novel NASICON-typed Na4VMn0.5Fe0.5(PO4)3 cathode for high-performance Na-ion batteries, Adv. Energy Mater. 11 (22) (2021).

[28] P. Kaspar, et al., Characterization of polyvinylidene fluoride (PVDF) electrospun fibers doped by carbon flakes, Polymers (Basel) 12 (12) (Nov 24 2020).
[29] Y.C. Lu, et al., In situ ambient pressure X-ray photoelectron spectroscopy studies of lithium-oxygen redox reactions, Sci. Rep. 2 (2012) 715.
[30] V. Aravindan, J. Gnanaraj, Y.-S. Lee, S. Madhavi, LiMnPO4 – a next generation cathode material for lithium-ion batteries, J. Mater. Chem. A 1 (11) (2013).
[31] X. Liu, et al., Stress- and interface-compatible red phosphorus anode for high-energy and durable sodium-ion batteries, ACS Energy Lett. 6 (2) (2021) 547–556.
[32] B. Peng, Y. Xu, K. Liu, X. Wang, F.M. Mulder, High-performance and low-cost sodium-ion anode based on a facile black phosphorus carbon nanocomposite, ChemElectroChem 4 (9) (2017) 2140–2144.
[33] R. Tatara, et al., The effect of electrode-electrolyte interface on the electrochemical impedance spectra for positive electrode in Li-ion battery, J. Electrochem. Soc. 166 (3) (2018) A5090–A5098.
[34] S. Abdalla, A. Obaid, F.M. Al-Marzouki, Preparation and characterization of poly (vinylidene fluoride): a high dielectric performance nano-composite for electrical storage, Results Phys. 6 (2016) 617–626.
[35] B.G. Lee, Y.J. Park, Enhanced electrochemical performance of lithia/Li2RuO3 cathode by adding tris(trimethylsilyl)borate as electrolyte additive, Sci. Rep. 10 (1) (Aug 11 2020) 13498.
[36] J. Cha, J.-G. Han, J. Hwang, J. Cho, N.-S. Choi, Mechanisms for electrochemical performance enhancement by the salt-type electrolyte additive, lithium difluoro (oxalato)borate, in high-voltage lithium-ion batteries, J. Power Sources 357 (2017) 97–106.
[37] S. Wang, H. Xu, W. Li, A. Dolocan, A. Manthiram, Interfacial chemistry in solid-state batteries: formation of interphase and its consequences, J. Am. Chem. Soc. 140 (1) (Jan 10 2018) 250–257.
[38] L. Bodenes, A. Darwiche, L. Monconduit, H. Martinez, The solid electrolyte interphase a key parameter of the high performance of Sb in sodium-ion batteries: comparative X-ray photoelectron spectroscopy study of Sb/Na-ion and Sb/Li-ion batteries, J. Power Sources 273 (2015) 14–24.
[39] J. Lee, et al., Tuning two interfaces with fluoroethylene carbonate electrolytes for high-performance Li/LCO batteries, ACS Omega 4 (2) (Feb 28 2019) 3220–3227.
[40] J. Zheng, et al., Highly stable operation of lithium metal batteries enabled by the formation of a transient high-concentration electrolyte layer, Adv. Energy Mater. 6 (8) (2016).
[41] M. Chen, et al., NASICON-type air-stable and all-climate cathode for sodium-ion batteries with low cost and high-power density, Nat. Commun. 10 (1) (Apr 1 2019) 1480.
[42] C. Marino, M. El Kazzi, E.J. Berg, M. He, C. Villevieille, Interface and safety properties of phosphorus-based negative electrodes in Li-ion batteries, Chem. Mater. 29 (17) (2017) 7151–7158.
[43] S. Park, et al., Replacing conventional battery electrolyte additives with dioxolone derivatives for high-energy-density lithium-ion batteries, Nat. Commun. 12 (1) (Feb 5 2021) 838.